Immuno-PET identifies the myeloid compartment as a key contributor to the outcome of the antitumor response under PD-1 blockade

Immuno-PET identifies the myeloid compartment as a key contributor to the outcome of the antitumor response under PD-1 blockade

Mohammad Rashidian[a,b,c], Martin W. LaFleur[d,e], Vincent L. Verschoor[a,b], Anushka Dongre[f], Yun Zhang[f], Thao H. Nguyen[d,e], Stephen Kolifrath[a,b], Amir R. Aref[g,h], Christie J. Lau[g,h], Cloud P. Paweletz[g,h], Xia Bu[g], Gordon J. Freeman[g], M. Inmaculada Barrasa[f], Robert A. Weinberg[f,i], Arlene H. Sharpe[d,e,j], and Hidde L. Ploegh[a,b,1]

[a]Program in Cellular and Molecular Medicine, Boston Children's Hospital, Boston, MA 02115; [b]Department of Pediatrics, Harvard Medical School, Boston, MA 02115; [c]Department of Imaging, Dana-Farber Cancer Institute, Boston, MA 02215; [d]Department of Immunology, Blavatnik Institute, Harvard Medical School, Boston, MA 02115; [e]Evergrande Center for Immunologic Diseases, Brigham and Women's Hospital, Harvard Medical School, Boston, MA 02115; [f]Whitehead Institute for Biomedical Research, Cambridge, MA 02142; [g]Department of Medical Oncology, Dana-Farber Cancer Institute, Boston, MA 02215; [h]Belfer Center for Applied Cancer Science, Dana-Farber Cancer Institute, Boston, MA 02215; [i]Department of Biology, Massachusetts Institute of Technology, Cambridge MA 02139; and [j]Department of Pathology, Brigham and Women's Hospital, Harvard Medical School, Boston, MA 02115

Contributed by Hidde L. Ploegh, June 27, 2019 (sent for review March 22, 2019; reviewed by Thomas F. Gajewski and Robert D. Schreiber)

Immunotherapy using checkpoint-blocking antibodies against PD-1 has produced impressive results in a wide range of cancers. However, the response remains heterogeneous among patients. We used noninvasive immuno-positron emission tomography (PET), using ^{89}Zr-labeled PEGylated single-domain antibody fragments (nanobodies or VHHs), to explore the dynamics and distribution of intratumoral CD8$^+$ T cells and CD11b$^+$ myeloid cells in response to anti–PD-1 treatment in the MC38 colorectal mouse adenocarcinoma model. Responding and nonresponding tumors showed consistent differences in the distribution of CD8$^+$ and CD11b$^+$ cells. Anti–PD-1 treatment mobilized CD8$^+$ T cells from the tumor periphery to a more central location. Only those tumors fully infiltrated by CD8$^+$ T cells went on to complete resolution. All tumors contained CD11b$^+$ myeloid cells from the outset of treatment, with later recruitment of additional CD11b$^+$ cells. As tumors grew, the distribution of intratumoral CD11b$^+$ cells became more heterogeneous. Shrinkage of tumors in responders correlated with an increase in the CD11b$^+$ population in the center of the tumors. The changes in distribution of CD8$^+$ and CD11b$^+$ cells, as assessed by PET, served as biomarkers to gauge the efficacy of anti–PD-1 treatment. Single-cell RNA sequencing of RNA from intratumoral CD45$^+$ cells showed that CD11b$^+$ cells in responders and nonresponders were markedly different. The responders exhibited a dominant population of macrophages with an M1-like signature, while the CD45$^+$ population in the nonresponders displayed an M2-like transcriptional signature. Thus, by using immuno-PET and single-cell RNA sequencing, we show that anti–PD-1 treatment not only affects interactions of CD8$^+$ T cells with the tumor but also impacts the intratumoral myeloid compartment.

PET imaging | checkpoint blockade | tumor immune microenvironment | nanobodies | single-cell RNA sequencing

Tumor cells, diverse populations of immune cells, and stromal fibroblasts engage in complex interactions within the tumor microenvironment (TME) (1–3). Treatment with antibodies that target immune checkpoints, such as PD-1/PD-L1 and CTLA-4, reshapes the TME; for example, by reactivating functionally exhausted CD8$^+$ cytotoxic T cells and/or preventing T-cell exhaustion. However, the impact of such treatments on other immune cell subpopulations, in particular those of the myeloid compartment, has been explored less. Similarly, the dynamics of different subpopulations of immune cells in response to anti-checkpoint treatment are not well studied, and have thus far defied noninvasive longitudinal monitoring.

The infiltration status of CD8$^+$ T cells in the TME in several tumor models, as assessed by conventional immunohistochemistry, correlates well with the response to CTLA-4 checkpoint blockade (4–6). Noninvasive imaging using immuno-positron emission tomography (PET) (7, 8) has also proven informative. Tumors with preexisting and homogeneously distributed CD8$^+$ T cells at diagnosis are more likely to respond to anti–CTLA-4 treatment, whereas tumors with a heterogeneous CD8$^+$ T-cell distribution respond less well (7).

Both CTLA-4 blockade and disruption of the PD-1/PD-L1 axis can improve antitumor immune responses through their impact on T cells. While PD-1 and CTLA-4 signaling might ultimately converge on common signaling pathways, the underlying mechanisms are distinct (9, 10). This raises the question of whether immuno-PET observations that have been made for anti–CTLA-4 treatment apply to anti–PD-1 treatment as well. We therefore investigated the dynamics of CD8$^+$ and CD11b$^+$ cell populations, 2 key players that shape the TME, in response to anti–PD-1 treatment in a mouse colon cancer model.

Significance

Immunotherapy, especially blockade of the PD-1/PD-L1 and CTLA-4 axes, has resulted in durable responses in a range of cancers. However, responses remain heterogeneous among patients. Treatment outcome results from changes in the tumor microenvironment imposed by such blockade. Here, we use immuno-PET and single-cell RNA sequencing to increase our understanding of the dynamics of immune cells and their functional status in the tumor microenvironment in response to PD-1 blockade. Our data provide insights into the dynamics of CD8$^+$ T cells and the functional status of the myeloid compartment in response to PD-1 blockade.

Author contributions: M.R. and H.L.P designed the study with help from M.W.L., X.B., G.J.F., R.A.W., and A.H.S.; M.R. performed experiments with help from all authors; M.W.L. performed flow cytometric analysis; M.R., V.L.V., and S.K. performed the PET imaging experiments; M.R., V.L.V., and S.K. analyzed data; T.N. performed CD8 immunostaining; A.D. performed immunostaining for EMT markers; M.R., A.D., and Y.Z. performed RNAseq experiments with help from the Whitehead Genome Technology Core facility; M.R. and M.I.B. analyzed the RNAseq data; A.A., C.J.L., and C.P.P. performed the tumor spheroid experiment; X.B. and G.J.F. contributed new reagents/analytic tools; R.A.W. and A.H.S. helped supervise the study; and M.R. and H.L.P. wrote the paper with help from all authors.

Reviewers: T.F.G., The University of Chicago; and R.D.S., Washington University School of Medicine in St. Louis.

The authors declare no conflict of interest.

[1]To whom correspondence may be addressed. Email: hidde.ploegh@childrens.harvard.edu.

This article contains supporting information online at www.pnas.org/lookup/suppl/doi:10.1073/pnas.1905005116/-/DCSupplemental.

Published online August 2, 2019.

Immuno-PET is a noninvasive method that can detect immune cells in vivo with a resolution of <1 mm. We developed radioisotopically labeled camelid single-domain antibody fragments (nanobodies or VHHs) that recognize surface markers on both lymphocytes and myeloid cells (11–13). Using sortase to site-specifically label VHHs with radioisotopes such as ^{18}F, ^{64}Cu, and ^{89}Zr, tumors <1 mm in diameter are detectable by virtue of the presence of infiltrating immune cells (11–13). In a B16 melanoma model in which only a fraction of animals respond to treatment with anti–CTLA-4 antibodies, immuno-PET reliably distinguished responders from nonresponders soon after the initiation of treatment (7). While the responders showed homogeneous infiltration of CD8$^+$ cells into the tumor core, nonresponders failed to do so and presented with heterogeneous distribution of the CD8$^+$ cells instead (7). We now show that immuno-PET can be used to monitor the responses to anti–PD-1 treatment in an anti–PD-1–responsive colorectal tumor model. Single-cell RNA sequencing (scRNAseq) analysis of intratumoral CD45$^+$ cells from animals that responded to anti–PD-1 treatment or failed to do so, identified by immuno-PET, documents an important role for the myeloid compartment in this response. This dataset also provides possible targets for intervention to improve the antitumor immune response.

Results

Using Immuno-PET to Explore Immune Cell Dynamics In Vivo. Using the mouse MC38 colorectal adenocarcinoma as an anti–PD-1–responsive tumor model (14), we applied ^{89}Zr-labeled PEGylated anti-CD8 and anti-CD11b VHHs to explore the dynamics of cytotoxic T cells and CD11b$^+$ cells, respectively (7), during anti–PD-1 blockade. Site-specific installation of a polyethylene glycol (PEG) moiety on a VHH can improve the signal-to-noise ratio and decrease kidney uptake, a common problem in immuno-PET when using antibody fragments (*SI Appendix*, Fig. S1) (7). As few as 70,000 CD8$^+$ T cells can be detected with an acceptable signal-to-background (muscle) ratio of 7:1 in a popliteal lymph node (*SI Appendix*, Fig. S1).

Responders to Anti–PD-1 Treatment Show Penetration of the Tumor by CD8$^+$ T Cells. We first investigated how anti–PD-1 treatment affects the dynamics of intratumoral CD8$^+$ T cells. After inoculation with MC38 cells (100,000 MC38-GFP$^+$ cells, s.c., below the right shoulder), mice were treated either with anti–PD-1 antibody or with an isotype control. Mice were imaged by PET, using ^{89}Zr-PEGylated anti-CD8 VHH before and after administration of anti–PD-1, to detect possible changes in CD8$^+$ T-cell distribution in response to treatment. PET images collected on day 8, just before the start of anti–PD-1 treatment, showed the presence of CD8$^+$ T cells within established tumors. However, most of this signal came from the tumor periphery, suggesting that the TME of the MC38 tumor does not readily allow penetration by, and intratumoral accumulation of, CD8$^+$ T cells (Fig. 1).

In the control cohort, tumors grew in size, with a persistently heterogeneous distribution of CD8$^+$ T cells and most of the CD8 signal continuing to derive from the tumor periphery. However, in the anti–PD-1–treated cohort, we noted a marked increase in the numbers of CD8$^+$ T cells that had migrated into the tumor already within 4 d after the initial dose of anti–PD-1 antibody (Fig. 1*C*, compare day 8 and day 12). On day 16, tumors had shrunk and were filled with CD8$^+$ T cells (Fig. 1*C*, day 16). In all cases, every shrinking tumor was filled with CD8$^+$ T cells, showing a strong signal from the core of the tumor ($n = 7$). Analyses of tumor samples by flow cytometry at necropsy confirmed the presence of CD8$^+$ T cells (*SI Appendix*, Fig. S2). Hence, effective anti–PD-1 treatment of the MC38 tumors was accompanied by infiltration of the tumor core by CD8$^+$ cells.

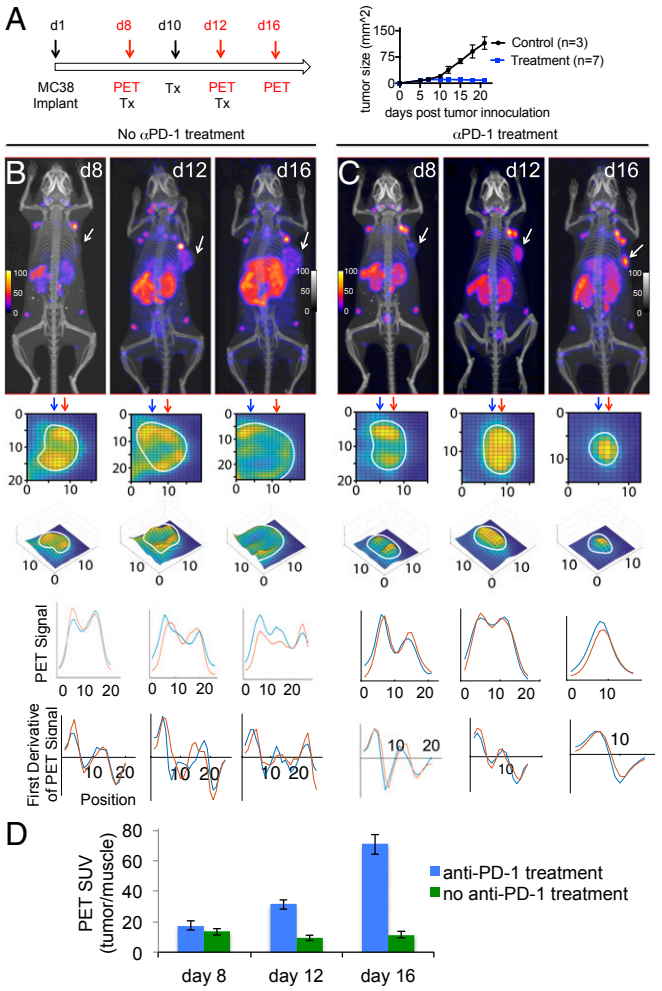

Fig. 1. Monitoring the dynamics of CD8$^+$ T cells in response to anti–PD-1 (αPD-1) treatment. (*A*) Schedule for the treatment and PET imaging. Animals were inoculated with 100,000 MC38-GFP$^+$ cells, s.c., below the right shoulder, and were treated either with anti–PD-1 antibody (200 μg per mouse, on days 8, 10, 12; $n = 7$) or with an isotype control ($n = 3$). (*B* and *C*) PET-CT images of MC38 tumor-bearing mice that received αPD-1 treatment and their controls. Panels below the PET-CT images are enlarged zoomed-in pictures of a cross-section of the tumor, to better visualize infiltration status of CD8$^+$ cells. For the control cohort (*B*), CD8$^+$ cells did not infiltrate into the core of the tumors. For the cohort treated with αPD-1, CD8$^+$ cells infiltrated the core of the tumor. Below the PET images are shown PET signal intensities and their first derivatives (below each graph). Two different columns, as indicated with the blue and red arrows, were picked, and graphs were drawn to show the local minima and maxima. The CD8 T-cell signal was more homogenously distributed in mice responding to PD-1 treatment with no local minima throughout the tumor (day 16), whereas partial responders showed a more heterogeneous signal distribution with 1 or more local minima. (*D*) Tumor PET signals in vivo for the indicated experiments in *B* and *C*.

A Cohort of Responders and Nonresponders Confirms the Predictive Value of CD8$^+$ T-Cell Distribution Assessed by Immuno-PET. Most MC38-bearing animals (6/7) showed a complete response to anti–PD-1 when treatment was begun early (tumors not larger than ∼3 to 4 mm in diameter) and involved a relatively high dose of antibody. To obtain a more variable response, we decreased the amount of anti–PD-1. Under these conditions, only about half the mice cleared the tumor (39/86 mice responded across all experiments; Fig. 2*A*).

To investigate how the TME of responders differed from that of nonresponders in this cohort, we imaged individual mice by immuno-PET at various points. In the treatment cohort, both

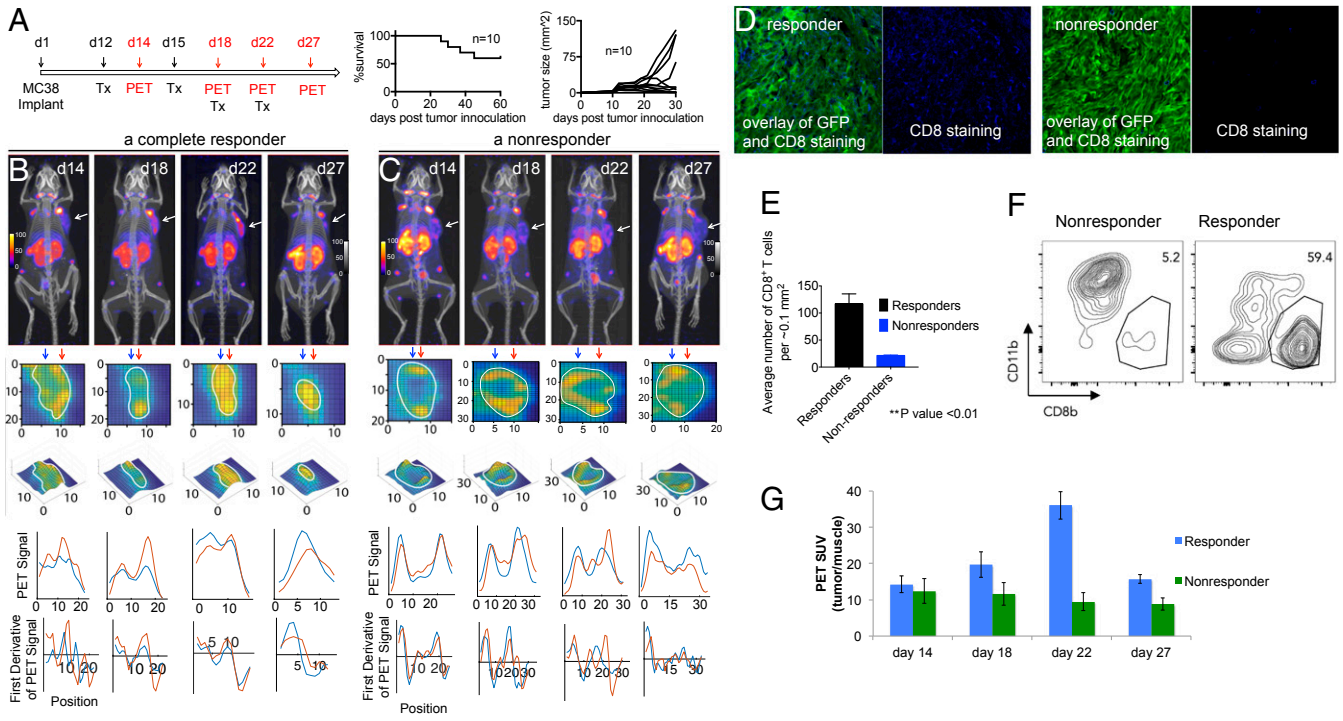

Fig. 2. Monitoring the dynamics of CD8$^+$ T cells in responder and nonresponder tumors. (*A*) Treatment schedule that yields a heterogeneous response, and the accompanying PET-CT imaging. Animals were inoculated with 50,000 MC38-GFP$^+$ cells, s.c., below the right shoulder, and were treated either with a suboptimal dose of anti–PD-1 antibody (100 μg per mouse, on days 12, 15, 18, and 22; 39/86 mice responded across all experiments) or with an isotype control (0/10 responded across all experiments). Only animals that had tumors larger than ∼3 mm in diameter on the first day of treatment were included. Animals that did not grow tumors or had tumors smaller than ∼3 mm in diameter on the first day of treatment were excluded (7 mice across all experiments). (*Right*) Survival curve. Mice were killed when tumors reached 2 cm in diameter or on ulceration. (*B* and *C*) PET-CT images of MC38 tumor-bearing mice that responded or failed to respond to anti–PD-1 treatment. Panels below the PET-CT images are zoomed-in pictures of a cross-section of the tumors to better visualize infiltration status of CD8$^+$ cells. For complete responders (*B*), CD8$^+$ cells populated the core of tumors. For the nonresponders (*C*), CD8$^+$ cells failed to infiltrate the tumor core; their intratumoral distribution remained heterogeneous at all points. Below the PET images are shown PET signal intensities and their first derivatives (below each graph). Two different columns, as indicated with the blue and red arrows, were picked, and graphs were drawn to show the local minima and maxima. The CD8 T-cell signal was more homogenously distributed in mice responding to PD-1 treatment with no local minima throughout the tumor (day 27), whereas partial responders showed a more heterogeneous signal distribution with 1 or more local minima. (*D*) Immunofluorescence imaging (CD8$^+$ cells) of frozen tumor sections shows infiltration of CD8$^+$ T cells into the responder tumors. For nonresponders, CD8$^+$ cells remained mostly peripheral. (*Left*) Overlay of the MC38-GFP$^+$ (green) and CD8 (blue) stains. (*Right*) CD8 stains (blue). (*E*) The CD8$^+$ T-cell numbers, calculated based on the average of several squares plotted randomly in different areas of the tumor ($n = 3$ for each cohort). (*F*) Flow cytometric analysis shows that more CD8$^+$ cells infiltrated the tumors in responders compared with nonresponders (data representative of $n = 3$ for each cohort). (*G*) Tumor PET signals in vivo for the indicated experiments in *B* and *C*.

nonresponders and partial responders showed some infiltration and expansion of CD8$^+$ T cells in the tumor. However, at no time during treatment did nonresponders show homogeneous infiltration of the tumor by CD8$^+$ T cells. In contrast, tumors in responders showed extensive infiltration by CD8$^+$ T cells soon after the start of anti–PD-1 treatment (Fig. 2 *B* and *C*). As visualized by immuno-PET, treatment with anti–PD-1 antibody not only induced expansion of CD8$^+$ T cells, but also mobilized them from the periphery to the core of each tumor, where their presence correlated with a complete response.

To further confirm our PET observations, we stratified responders and nonresponders by immuno-PET, based on the distribution of CD8$^+$ T cells. We then excised their tumors and analyzed them by immunohistochemistry and flow cytometry. This confirmed the presence of more CD8$^+$ T cells in tumors of responders than in nonresponders (Fig. 2 *D*–*F*).

Blockade of Lymphocyte Trafficking Impedes the Anti-Tumor Response. To distinguish the contribution of CD8$^+$ T cells present in the tumor ab initio from CD8$^+$ T cells newly recruited in response to anti–PD-1 treatment, we used FTY720, an inhibitor of the sphingosine-1-phosphate receptor, which regulates immune cell trafficking, to block egress of T cells from lymphoid organs, thereby preventing them from infiltrating peripheral tissues (15). As reported by others, administration of FTY720 yields a decrease of up to 90% of circulating T cells (16). We treated tumor-bearing mice with FTY720 according to the schedule shown in Fig. 3*A*. The first cohort received FTY720 1 d before tumor inoculation (day 0), which should have lowered the numbers of intratumoral CD8$^+$ T cells before the start of anti–PD-1 treatment. The second cohort received FTY720 on day 7, 1 d before the start of anti–PD-1 treatment; in these animals, a number of CD8$^+$ T cells should already be present in the tumor, while far fewer additional T cells are expected to enter the tumor from the circulation thereafter. The control cohort received no FTY720.

Cohorts receiving FTY720 at day 0 or day 7 showed either a weak or no response to treatment with anti–PD-1, as gauged by tumor volume and survival, indicating that FTY720 effectively prevents the response to anti–PD-1 treatment when applied sufficiently early (Fig. 3*B*). This suggested that communication between secondary lymphoid organs and the MC38 TME was needed to adequately respond to anti–PD-1 treatment. We also imaged tumor-bearing animals by PET-CT, using anti-CD8 ^{89}Zr-PEG20-VHH, at 11 and 20 d postinoculation. In the cohorts that received FTY720, infiltration of CD8$^+$ T cells in the TME remained heterogeneous, with little or no infiltration into the cores of these

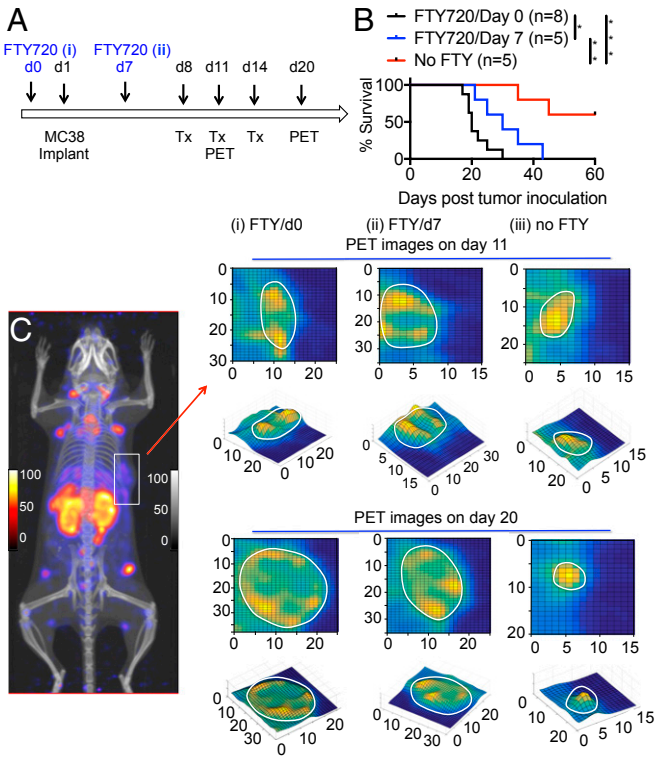

Fig. 3. The effect of FTY720 treatment on dynamics and distribution of $CD8^+$ cells in response to anti–PD-1 (αPD-1) treatment. (*A*) MC38 tumor-bearing mice were treated with FTY720 twice a week, at 20 μg per mouse, starting either at day 0 (cohort i, $n = 8$) or day 7 (cohort ii, $n = 5$). The control cohort (cohort iii) did not receive FTY720 ($n = 5$). Mice were treated with αPD-1 and were subjected to PET-CT imaging according to the schedule shown in A (10^5 MC38-GFP$^+$ cells were injected at day 1 followed by a sub-optimal dose of treatment to maximize the effect of FTY720 treatment; 100 μg αPD-1 antibody on days 8, 11, and 14). (*B*) Survival curves for each of the 3 cohorts. Mice were killed when tumors reached 2 cm in diameter or on ulceration. Log-rank statistical test was performed to determine significance between each cohort (*$P < 0.05$; **$P < 0.01$; ***$P < 0.001$). (*C*) PET-CT maximum intensity projection images of a B6 mouse, injected with αCD8 ^{89}Zr-PEG20-VHH, 11 d after inoculation of the MC38 tumor (box); for each of the cohorts that received FTY720 (*C*, *i* and *ii*) and the control cohort (*C*, *iii*), PET images of a cross-section of the tumors on days 11 and 20 are shown: (*Top*) day 11, (*Bottom*) day 20 after tumor inoculation. Tumors, as identified by CT, are marked by the outline. The PET signals in the tumor are rendered as a heat map. Below each image is the corresponding 3D rendition, in which the *z* axis represents the strength of the PET signal in arbitrary units.

tumors. However, in animals that received no FTY720, the tumors of responders shrank and were indeed filled with $CD8^+$ T cells, consistent with our earlier observations (Fig. 3*C*).

$CD11b^+$ and $CD8^+$ Cells Show Different Intratumoral Distributions in the Course of Anti–PD-1 Treatment. $CD11b^+$ cells in the tumor microenvironment comprise a heterogeneous set of leukocytes, including monocytes, neutrophils, natural killer cells, granulocytes, and macrophages. In the case of the latter, the $CD11b^+$ myeloid-derived suppressor cells dampen immune responses and favor tumor growth, differentiation, and metastasis. In contrast, $CD11b^+$ M1-type macrophages have antitumor activity. However, this M1-M2 dichotomy is likely an oversimplification that does not do justice to the phenotypic and functional heterogeneity of macrophages more generally (17–19).

To better understand how anti–PD-1 treatment affects the $CD11b^+$ population, we performed immuno-PET, using an anti-CD11b VHH (11). We monitored the dynamics of $CD11b^+$ cells in the MC38 tumor model in response to anti–PD-1 treatment and imaged mice on days 8, 12, and 16 posttumor inoculation. In contrast to $CD8^+$ T cells, $CD11b^+$ cells were present throughout the tumor before treatment (compare infiltration of $CD8^+$ cells in Fig. 1*B* and $CD11b^+$ cells in Fig. 4*B* in the tumors for the images obtained on day 8). In tumors that continued to grow, the distribution of $CD11b^+$ cells became more heterogeneous. Upon necropsy and regardless of treatment, none of the tumors showed necrotic sections. In responders, however, the shrinking tumors showed a homogeneous distribution of PET signal, suggesting that $CD11b^+$ cells were evenly distributed throughout the tumor (Fig. 4*B*, day 16). The cellular composition of the already heterogeneous $CD11b^+$ pool may well change in the course of tumor growth and in response to anti–PD-1 treatment.

Of note, our images cannot distinguish among $CD11b^+$ NK cells, macrophages, and neutrophils based on the anti-CD11b PET signal, a possibility to which we return when discussing the data from scRNAseq experiments on intratumoral $CD45^+$ cells. Overall, the CD11b PET data suggest that tumors are effective at attracting $CD11b^+$ cells, but not $CD8^+$ T cells, into the tumor core, even before treatment.

3D Microfluidic Ex Vivo Culture of Organotypic Tumor Spheroids Captures the Difference between Responders and Nonresponders. To better characterize and understand the TME of responders and nonresponders, we prepared tumor spheroids grown in 3D cultures in vitro. These closely model the microenvironment of the tumor in vivo (20, 21). Such spheroids, prepared as reported

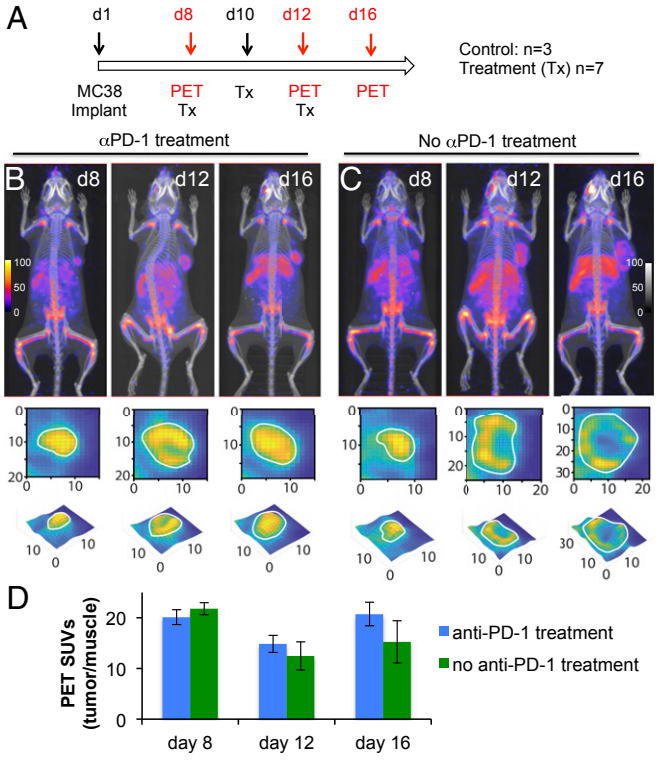

Fig. 4. Monitoring the dynamics of $CD11b^+$ cells in responders and nonresponders. (*A*) Schedule for anti–PD-1 (αPD-1) treatment and PET-CT imaging. Animals were inoculated with 100,000 MC38-GFP$^+$ cells, s.c., below the right shoulder, and were treated either with anti–PD-1 antibody (200 μg per mouse, on days 8, 10, and 12; $n = 7$) or with an isotype control ($n = 3$). (*B* and *C*) PET-CT images of MC38 tumor-bearing mice of the 2 cohorts. Panels below the PET-CT images are enlarged zoomed-in pictures of a cross-section of the tumors, to better visualize infiltration status of $CD11b^+$ cells in the tumors. (*D*) Tumor PET signals in vivo for the indicated experiment in *B* and *C*.

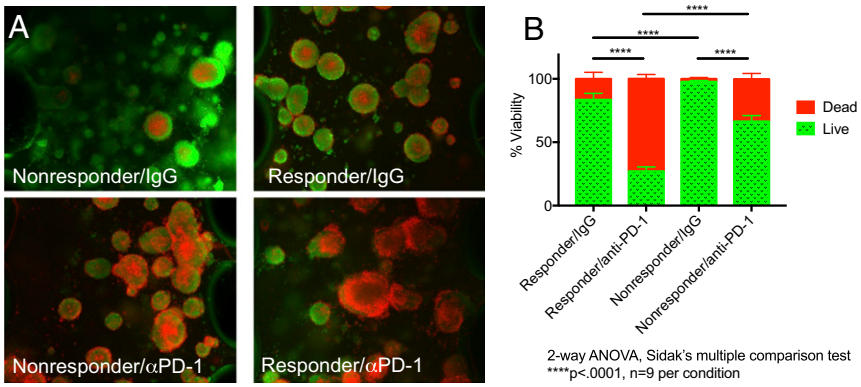

Fig. 5. Live/dead imaging and analysis of murine-derived organotypic tumor spheroids (MDOTS). (*A*) Acridine orange and propidium iodide staining of MC38 MDOTS on day 6 of ex vivo culture, comparing control (isotype control IgG, 10 μg/mL; $n = 9$) with anti–PD-1 (10 μg/mL; $n = 9$). (*B*) Live/dead analysis of MC38 MDOTS treated with IgG or anti–PD-1 (10 μg/mL) for 6 d in 3D microfluidic culture. A 2-way ANOVA followed by Sidak's multiple comparisons test was performed to determine significance between each of the 4 conditions.

(20), consist of 40- to 100-μm-diameter tumor cell clusters and contain MC38 cancer cells, fibroblasts, and immune cells. They allow a distinction between dead and live cells, thereby complementing our PET observations.

We prepared tumor spheroids from responder and nonresponder animals that received anti–PD-1 treatment, in which responses were identified via CD8 immunoPET, as explained in Fig. 2. Spheroids were treated in culture with either anti–PD-1 IgG or an isotype control IgG (10 μg/mL IgG or 10 μg/mL anti–PD-1). Live and dead cells were enumerated 6 d later. We observed a significant increase in the number of dead MC38 cells among spheroids prepared from the responder tumors, consistent with the response to anti–PD-1 treatment (Fig. 5). We observed more MC38 dead cells in the responder spheroids even when they had received control IgG. The antitumor status of the TME of responders, even without adding the anti–PD-1 antibody to the spheroid cultures, permitted killing of more MC38 tumor cells, in line with the observation and predictions of PET data (Fig. 5).

Exploring Epithelial and Mesenchymal Characteristics of the MC38 Cancer Cells in Responders and Nonresponders. The epithelial and mesenchymal characteristics of a tumor can determine the response to checkpoint blockade (22–24). While tumor cells with epithelial traits recruit immune cells with antitumor properties, their more mesenchymal counterparts attract immunosuppressive cells instead. In 2 MMTV-PyMT–derived mammary carcinoma cell models, the more mesenchymal variants were resistant to anti–CTLA-4 checkpoint blockade, while the epithelial variants were sensitive. Anti–CTLA-4 treatment did not affect the persistence of carcinoma cells in the more mesenchymal state (22).

To determine whether anti–PD-1 treatment affected epithelial or mesenchymal characteristics of the MC38 tumor cells in vivo, we performed histology and immunostaining on responder and nonresponder tumor samples, and also on samples that did not receive anti–PD-1 treatment. All 3 samples showed mesenchymal characteristics, as indicated by the strong expression of vimentin and nuclear staining for Zeb1, a key transcription factor that marks the activation of the epithelial–mesenchymal transition and the formation of more mesenchymal carcinoma cells (Fig. 6*A*). Moreover, the less differentiated morphology of the cancer cells also suggested a more mesenchymal phenotype. The carcinoma cells, identified by their expression of GFP (MC38-GFP$^+$), did not show detectable levels of expression for

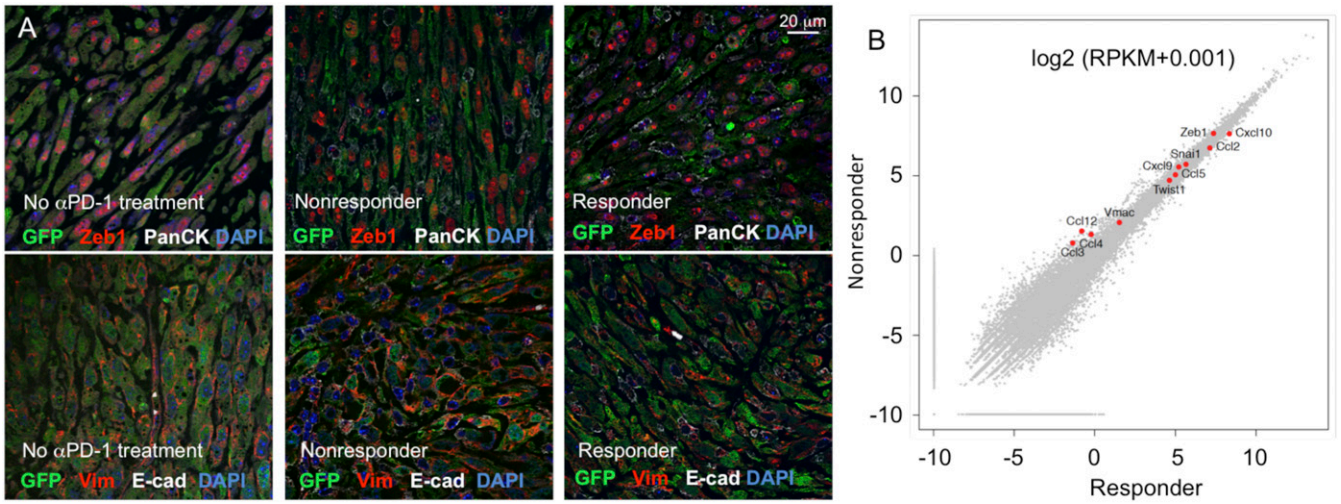

Fig. 6. Exploring differences in the cancer cells in responders and nonresponders. (*A*) Immunofluorescence staining for epithelial-mesenchymal transition markers expressed by cells in the responder and nonresponder tumors, and tumors that did not receive anti–PD-1 treatment ($n = 3$ for each cohort). (*B*) RNAseq analysis on the MC38 cancer cells sorted from responder and nonresponder tumors ($n = 2$ for each cohort).

E-cadherin and cytokeratins, indicating that these carcinoma cells were mostly mesenchymal, regardless of treatment outcome (Fig. 6*A*). Furthermore, bulk RNAseq analysis on the tumor cancer cells sorted from responders and nonresponders showed expression of mesenchymal markers (Fig. 6*B*). Thus, the results suggest that response to at least 1 form of checkpoint blockade did not alter the residence of carcinoma cells in the mesenchymal state.

Characterizing Transcriptome of the MC38 Cancer Cells in Responders and Nonresponders. RNAseq analysis of bulk populations of MC38-GFP$^+$ carcinoma cells (sorted from tumors for GFP$^+$ cells) showed that their transcriptomes are not affected in a major way by the response to checkpoint blockade (Fig. 6*B*). However, we noted some differences, including a 5-fold increase in nonresponders for CCL12 transcripts, which encode a chemoattractant for monocytes. Analysis of the tumor-infiltrating CD45$^+$ cells by scRNAseq showed higher levels of CXCR2 transcripts (CCL12 receptor) in the nonresponders (Fig. 7*D*).

scRNAseq on CD45$^+$ Cells from a Responder and a Nonresponder Show Marked Differences in the Transcriptomes of the Myeloid Compartment. To better characterize and understand the tumor immune microenvironment, we sorted CD45$^+$ cells from nonresponding and responding tumors as identified by immuno-PET and subjected them to scRNAseq (~3,500 cells per sample). A near-complete lack of overlap in PCA-based tSNE plots for the CD45$^+$ compartments of these 2 populations showed that the myeloid populations, identified as positive for CD11b transcripts, in responders and nonresponders differed in their transcriptomic profiles (Fig. 7*A*). The difference between responders and nonresponders, as identified by immuno-PET, correlated with an equally clear dichotomy in transcript profiles. This underscores the utility of immuno-PET imaging of CD8$^+$ T cells as a method to gauge the efficacy of ongoing anti–PD-1 treatment.

To match the subpopulations of cells common to responder and nonresponder tumors, and to compare gene expression profiles, we aligned both datasets, using canonical correlation analysis (CCA) (Fig. 7*B*) (25). CCA identifies gene-gene correlation patterns that are conserved across the datasets and uses these patterns to align the 2 groups, so that similar cell types in both groups can be matched. CCA followed by CCA-based tSNE analysis, using the aligned canonical components as input, identified 10 clusters (Fig. 7 *B* and *C*). Cluster 5 contained CD8$^+$ cells characterized by high levels of CD3γ, CD8, and other T-cell markers. The other clusters correspond to myeloid cells, mostly macrophages and dendritic cells, but the gene signatures that characterize them are sufficiently similar to preclude assignment to unique and distinct macrophage or dendritic cell (sub)types. Cluster 9 contained only 43 cells and was not included in further analysis.

Myeloid cells from the nonresponder tumor showed increased expression of genes associated with M2 polarization (19) (Fig. 7*D*). We observed higher levels of transcripts encoding secreted phosphoprotein 1 (26-fold average increase) and fibronectin (12-fold average increase) in nonresponders (Fig. 7*D*); secreted phosphoprotein 1 plays an important role in macrophage polarization and immune escape (26). Moreover, only alternatively activated macrophages express fibronectin when stimulated by IL-4 or glucocorticoids instead of IFNγ or lipopolysaccharide (27). Prostaglandin G/H synthase 1 transcripts were also significantly higher in nonresponder CD45$^+$ cells (3.3-fold). This enzyme

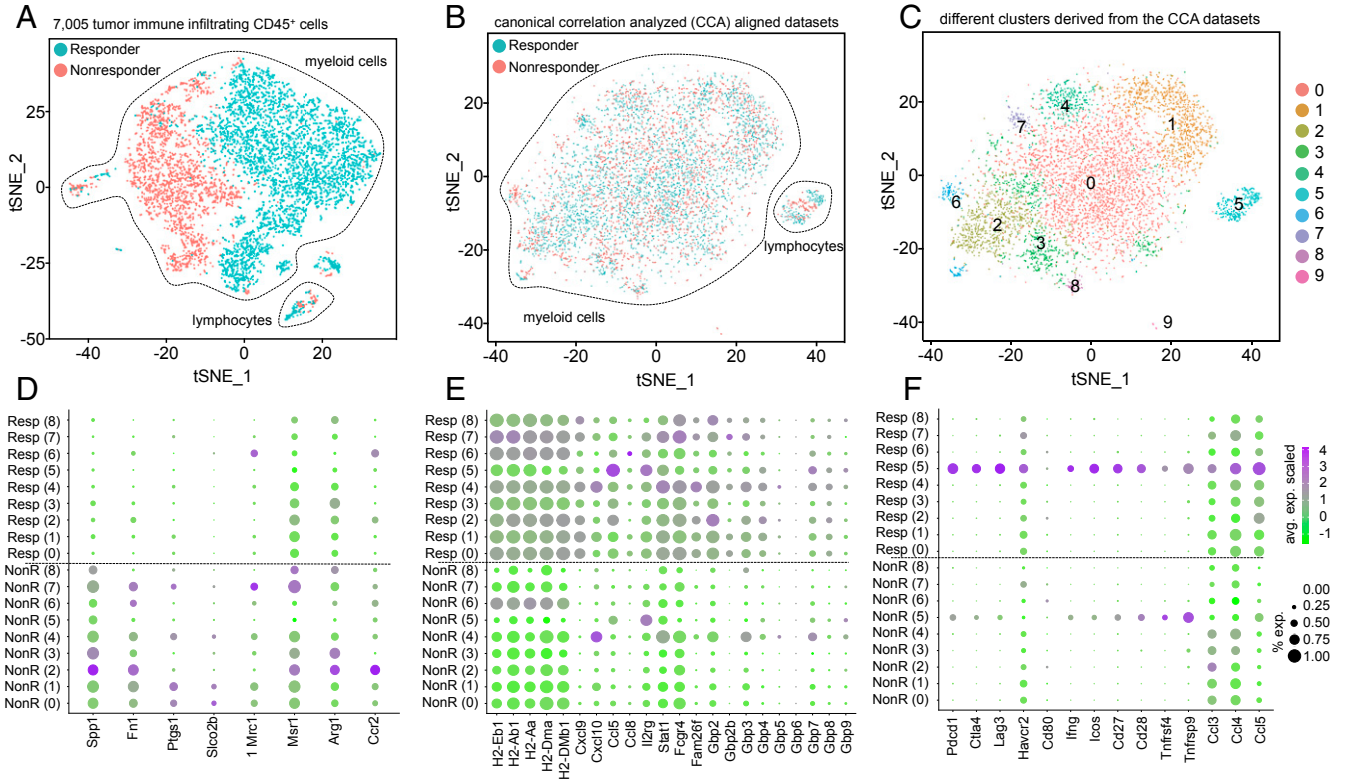

Fig. 7. Single-cell RNAseq analysis on the immune (CD45$^+$) infiltrating cells in responder and nonresponder tumors. tSNE plots of responder and nonresponder myeloid cells show (*A*) initial near-complete separation before (*B*) alignment with CCA. (*C*) Clusters found on the immune infiltrating cells (post-CCA). (*D*–*F*) Transcript metrics (average scaled level and percentage of expressing cells) of selected myeloid cell genes in responder and nonresponder cells from clusters 0 to 8 are shown for genes that exhibit higher levels in (*D*) nonresponder myeloid cells, (*E*) responder myeloid cells, and (*F*) responder lymphocytes. Each number (0 to 8) represents a cell cluster.

generates prostaglandin E2 (PGE2), a known contributor to an immunosuppressive TME. Likewise, transcripts for Solute carrier organic anion transporter family member 2B1, which mediates Na^+-independent transport of organic anions such as the prostaglandins PGD2, PGE1, and PGE2, were highly up-regulated in nonresponder $CD45^+$ myeloid cells (12-fold). We also observed more modest increases in CD206 (Mrc1; 3.4-fold), CD204 (Msr1; 1.8-fold), and arginase-1 (Arg1; 5-fold) transcripts, which are genes commonly associated with M2 polarization (Fig. 7*D*). Thus, the myeloid compartment in the nonresponder tumors dampens the antitumor immune response and supports tumor growth.

Relative to myeloid cells from unresponsive tumors, those extracted from tumors responsive to anti–PD-1 treatment showed elevated levels of transcripts that encode class II MHC (H2-Eb1 [3.7-fold], H2-Ab1 [3.9-fold], H2-Aa [3.4-fold], H2-DMa [2.1-fold], H2-DMb1 [3.2-fold]), CXCL9 (12-fold), CXCL10 (~2-fold in clusters 0, 1, and 2), CCL5 (4.6-fold), CCL8 (5-fold), IL2rg (the γ chain common to the IL-2, IL-4, IL-7, IL-15, and IL-21 receptors; 2.4-fold), Stat1 (2.3-fold), Fcgr4 (4.6-fold), and Fam26f (9.5-fold; Fig. 7*E*). Thus, it appears that macrophages with an M1-type signature help polarize the TME toward an antitumor status.

Guanylate-binding protein (GBP)-5 is a marker of IFNγ-induced, classically activated human macrophages (28). Although our study is focused on a murine model, we saw significantly higher levels of GBP transcripts in responding tumors, including those of GBP2 (4-fold), GBP2b (50.6-fold), GBP3, GBP4, GBP5, GBP6, GBP7, GBP8, and GBP9 on $CD45^+$ cells, with GBP2b present exclusively in responders (Fig. 7*E*). This provided an additional indication that macrophages in the TME of the responder are polarized toward M1 antitumor status. Moreover, this suggested that GBP2 or GBP2b could serve as a marker of mouse, and perhaps also human, M1 macrophages (Fig. 7*E*).

Anti–PD-1 treatment can affect the $CD8^+$ T-cell population through expansion of a subpopulation of PD-1^+ antigen-specific $CD8^+$ T cells and by helping them remain in a more functional state (29). scRNAseq analysis afforded a closer look at the characteristics of $CD8^+$ T cells present in the responder and nonresponder tumors. Transcripts for checkpoint molecules were up in responder $CD8^+$ T cells: PD-1 (2.4-fold), CTLA-4 (3.1-fold), LAG3 (7.2-fold), Tim-3 (8.1-fold), and CD80 (2-fold). Negative feedback on the activation status of T cells could explain this result. Higher overall levels of IFNγ (3.2-fold higher) in the TME of the responder could contribute to this as well. Transcript levels for some of the costimulatory molecules, in particular ICOS, were likewise up in responder $CD8^+$ T cells, in line with their activation status and killing abilities: ICOS (3.5-fold) and CD27 (2.2-fold), were up, while CD28 (1.4-fold) was not very different and OX40 (0.5-fold) and CD137 (0.7-fold) were somewhat down (Fig. 7*F*).

Chemokine and Cytokine Transcript Levels in the Tumor Immune Microenvironment. Chemokines and cytokines shape the TME by their ability to recruit various immune cell populations, and by activating them through promotion of intercellular interactions. Macrophage inflammatory protein-1 family (MIP-1) and related proteins CCL3 (MIP-1α), CCL-4 (MIP-1β), and CCL5 (Rantes) can convert the TME to an antitumor environment. Thus, these cytokines recruit antigen-presenting cells, including the dendritic cells essential for priming and activation of T cells. In T cells of responders, the transcripts of these 3 cytokines were significantly elevated, relative to those present in nonresponders: CCL3 (3.8-fold), CCL4 (5.9-fold), and CCL5 (3.6-fold) (Fig. 7*F*).

CXCL9 and CXCL10 can recruit and activate $CD8^+$ T cells. Transcripts of both genes were elevated, especially those of CXCL9 (12 fold), in responder myeloid cells relative to nonresponder cells. T cells themselves did not express CXCL9 or CXCL10. Thus, the CXCL9 produced by $CD45^+$ myeloid cells in the responders might serve as an additional factor in establishing an antitumor environment in the context of anti–PD-1 treatment (Fig. 7 *E* and *F*). CCL3 regulates $CD8^+$–T-cell effector function and migration (30). We observed an increase (3.8 fold) of CCL3 transcripts in responder $CD8^+$ T cells. In the myeloid compartment, CCL3 and CCL4 transcripts were present at comparable levels in responders and nonresponders, while CCL5 was increased in responders (4.6-fold).

Discussion

PD-1 expressed by T cells affects their functional status, as shown by expansion of activated T cells upon blockade of PD-1 (31, 32). In line with recent similar findings (33), we show that anti–PD-1 treatment also reprograms $CD45^+$ cells in the TME to create a more favorable antitumor environment. Gubin et al. (33) showed that remodeling of both the lymphoid and myeloid intratumoral compartments occurs in response to checkpoint blockade. In experiments using the well-characterized T3 murine methylcholanthrene-induced sarcoma line, multiple subpopulations of macrophages and monocytes showed changes over time, as assessed by scRNAseq and by evaluation of protein expression using mass cytometry (CyTOF). A neutralizing anti-IFNγ antibody, when used in combination with PD-1 blockade, inhibited reprogramming of macrophages from M2-like to M1-like cells. The changes induced by such blockade therefore seem to be largely dependent on production of IFNγ by reinvigorated T cells (33).

Responses to checkpoint blockade are heterogeneous among patients. By monitoring the dynamics of $CD8^+$ T cells via immuno-PET, we can monitor progress of anti–PD-1 treatment. Anti–PD-1 treatment in responders is accompanied by an expansion and mobilization of $CD8^+$ T cells from the tumor periphery into the core of the tumor. Our findings are in line with those of Tumeh et al. (34). Biopsies of skin lesions from patients with metastatic melanoma and analyzed for $CD8^+$ T-cell infiltration status and clonality before and after PD-1 blockade treatment showed significant expansion of T cells in the TME in responders (34).

Interpretation of these observations is complicated by several factors. Due to the stochastic nature of the diversification of antigen-receptor repertoire and other poorly understood variables, the inbred mice will differ in their adaptive immune systems (35, 36). For an individual mouse, the specificity and numbers of T cells that can recognize the tumor are therefore impossible to predict, but could very well contribute to the observed differences between responders and nonresponders. We also should not discount the possible impact on the immune response when considering the numerous germline polymorphisms in other genes, even in inbred mice (37). Moreover, T cells of a given specificity may exert selective pressure on tumors, which might lead in turn to the outgrowth of tumor cells that have down-regulated antigen, resulting in intratumoral heterogeneity. While we assume that the MC38 cell inoculum is homogeneous, only detailed (epi)genomic and transcriptome analyses would address possible sources and degree of heterogeneity within a tumor that could affect its outgrowth.

In our model, we find that successful anti–PD-1 treatment requires timely recruitment of lymphocytes from the circulation when using a suboptimal dose of anti–PD-1. Spranger et al. (16) used a more vigorous treatment regimen, a combination of anti–CTLA-4 and anti–PD-1, in the immunogenic B16-dsRed-SIY model, and showed that after FTY720 treatment, the number of antigen-specific TILs increased (16). However, some loss of efficacy was observed at later times, suggesting that arrival of T cells from the periphery does contribute to an effective response.

We used RNAseq on the sorted MC38 cancer cells and scRNAseq on the sorted tumor infiltrating $CD45^+$ cells to identify molecular players that could contribute to treatment outcome. With the possible exception of CCL12, we saw no major changes in the transcriptomes of MC38 cells in responders and nonresponders (Fig. 6*B*). scRNAseq on $CD45^+$ cells showed higher

levels of CXCR2 transcripts (CCL12 receptor) in the nonresponder as well (Fig. 7*D*). This calls for further investigation on the roles of CCL12 and CXCR2. For example, blocking of CCL12 or CXCR2 might synergize with anti–PD-1 treatment (38).

How does the myeloid compartment change in the course of treatment, and do these changes affect outcome? The scRNAseq analysis on the tumor-infiltrating $CD45^+$ cells showed major differences between responder and nonresponder tumors, suggesting that the immune cells play a major role in the outcome of treatment. Both lymphocytes and myeloid cells in responder and nonresponder tumors (Fig. 7) showed major differences in their transcriptomes.

The $CD11b^+$ cells in nonresponders might well play a role in preventing entry of $CD8^+$ T cells into the tumor (39–41). Whether the change in myeloid status in the TME precedes or follows T-cell activation remains to be established. Production of IFNγ by T cells on checkpoint blockade might well drive these events (33).

Resistance to treatment with checkpoint-blocking antibodies is not well understood, and effective biomarkers are lacking. Our study provides a combination of markers that should prove useful in exploring the underlying causes of nonresponsiveness to checkpoint blockade in tumors more generally. Responses to checkpoint blockade are likely affected by both anatomical location of the tumor and the tissue origin of the targeted neoplastic cells. In addition, as we have shown here, the presence or absence and phenotype of various leukocytes affect the ultimate response to checkpoint immunotherapy. For this reason, it is essential to fully characterize and understand the entire immune profile of tumors, including the myeloid compartment, to develop more effective biomarkers and improve outcomes. Our findings call for more detailed studies of how anti–PD-1 treatment changes the status of the various components of the TME and in tumors of different histological origin.

As shown here, noninvasive imaging by immuno-PET can help monitor intratumoral $CD8^+$ T cells, even without knowing their specificity, and gauge the progression of the antitumor response to anti–PD-1 treatment. Such observations might inform better decisions on treatment options for patients. Our findings provide an impetus for similar studies in a clinical setting to determine whether comparable results could assist in the early identification of responders and nonresponders.

Materials and Methods

Mice. Animal studies were approved by the Boston Children's Hospital Committee on Animal Care (protocol 16-12-3328). Six- to 10-wk-old WT C57BL/6 female mice were used for all experiments. Mice were purchased from the Jackson Laboratory.

Tumor Cell Line, Implantation, and Treatment. MC38-GFP^+ adenocarcinoma (from Dr. A. Sharpe) was used for all experiments. Cells were cultured in vitro in Dulbecco's Modified Eagle Medium (DMEM) supplemented with 10% FBS. Mice were injected in the upper right shoulder s.c. with either 10^5 or 5×10^4 tumor cells, as explained in the figure legends. Tumors were measured every 2 to 3 d (length × width) with a caliper. Mice were killed when tumors reached 2 cm in diameter or upon ulceration. Where indicated, mice were given antibody i.p., using anti–PD-1 (clone 29F.1A12) or isotype control (clone 2A3 from BioXCell). Only animals that had tumors larger than ∼3 mm in diameter on the first day of treatment were included in the experiments. Animals that did not grow tumors or had tumors smaller than ∼3 mm in diameter on the first day of treatment were excluded. On collection, tumors were dissected and mechanically disaggregated before digestion with collagenase type I (400 U/mL; Worthington Biochemical) for 30 min at 37 °C. Next, tumors were passed through a 70-μm filter, followed by isolation of mononuclear cells via centrifugation through a Percoll gradient (40% and 70%). Flow cytometry was performed on a BD LSR II instrument. Antibodies were purchased from BioLegend and Thermo Fisher Scientific.

Preparation of Radiolabeled VHHs. Radiolabeling was performed after an established procedure (42). In a typical reaction, a solution of ∼50 ng of chelexed PEGylated-VHH-DFO in 200 μL of 0.5 M Hepes buffer, pH 7.5 was prepared. Then a volume of the $^{89}Zr^{4+}$ ion stock solution (typically supplied in 1.0 M oxalic acid) corresponding to ∼1.0 mCi was added to a 2 mL plastic screw-cap microcentrifuge tube. The pH of the $^{89}Zr^{4+}$ solution was adjusted to 6.8 to 7.5 using 2.0 M Na_2CO_3. This solution was added to PEG-VHH-DFO. The reaction mixture was incubated for 60 min at room temperature on an agitating block at 350 rpm, loaded onto a PD-10 size-exclusion cartridge (GE Healthcare), and eluted with 10 mL PBS, yielding >80% (∼0.8 mCi) of ^{89}Zr-PEGVHH (decay-corrected radiochemical yield). These methods were taken from ref. 7 (p. 2253) with minor changes.

PET-CT Studies. PET-CT procedures have been described in detail elsewhere (7). For imaging experiments, mice were anesthetized using 1.5% isoflurane in O_2 at a flow rate of ∼1 L/min. Mice were imaged by PET-CT using a G8 PET-CT small-animal scanner (PerkinElmer). Peak sensitivity of the G8 PET-CT accounts for >14% of positron emission, with a mean resolution of 1.4 mm. Each PET acquisition took 10 min, followed by a 1.5-min CT scan. Images were processed using the manufacturer's automatic image reconstruction software. Data were further analyzed and quantified using VivoQuant software. PET images were viewed side-by-side with the CT images in DICOM viewer software. Scans were sliced along the coronal plane. A representative image slice that best demonstrated the characteristics of immune cell infiltration for that particular sample was exported as a single DICOM file. Cartesian points that framed the tumor were recorded. The DICOM file was imported into MATLAB and processed with code that read the DICOM file and generated a matrix with PET signal values corresponding to each voxel. The Cartesian points recorded were used to crop the matrix to the tumor section only. The 3D shaded surface plots were generated using the MATLAB function surf, where the *x* and *y* axes represent points on the image plane and the *z* axis represents the PET signal value. For PET quantification, PET images were imported into VivoQuant software. PET signal values were converted into units of percentage of injected dose per gram by using as input the radioactivity at the time of measurement with the preprocessing tool. The CT scan overlaid with PET signal was used as a guide to generate 3D regions of interest (ROIs) to represent a certain organ within the mouse. Depending on the complexity of the ROI, drawing the ROIs was either done free-hand or in automated fashion by setting a threshold value, such that it would capture all connected points with a PET signal above the threshold value. Once all ROIs were generated, a table was exported containing statistical information, such as mean PET signal or variation, for each of the ROIs. To identify local minima and maxima of PET signal within a tumor, we used the same representative image slice used to generate the surface plot mentioned previously. We chose 2 line segments that intersected the middle of the tumor and used MATLAB to plot the signal intensity along the line segment. With the resulting plot, we approximated the first derivative by calculating the difference between adjacent values of signal intensity versus position on the line segment. A first derivative plot that crossed the *x* axis only once shows a single local maximum of the PET signal. In contrast, a plot that crossed the *x* axis 2 or more times indicates that the PET signal contained multiple local maxima or minima. These methods were taken from ref. 7 (p. 2253) with minor changes.

Immunostaining. Excised tumors were fixed in 4% paraformaldehyde/PBS at room temperature for 2 h. Next, the tumors were dehydrated in 30% sucrose/PBS solution overnight at 4 °C. The next day, tumors were embedded into optimal cutting temperature compound and then immediately frozen on dry ice and moved to −80 °C until sectioning was performed. For staining, tumors were sectioned at 14 μm, and slides were fixed in acetone for 10 min at −20 °C. Slides were washed with PBS and blocked with 10% FBS/PBS solution for 1 h. Primary anti-CD8 antibody (APC conjugated, clone #YTS156.7.7 BioLegend) and anti-GFP antibody (FITC-conjugated, Abcam, clone #Ab6662) were diluted in 2% FBS/PBS solution. Slides were stained for 1 h at room temperature with antibodies and washed 3 times in PBS afterward. Prolong Gold Antifade Mountant (Thermo Fisher, catalog #P10144) was applied directly onto tumor tissues that were subsequently dried overnight at room temperature in the dark. Next, images were taken with confocal microscope Olympus FV3000. The $CD8^+$ T cells counts were an average of several squares plotted randomly in different areas of the tumor.

Treatment with FTY720. Fingolimod (FTY720, Cayman Chemical) was given to animals to inhibit egress of lymphocytes from lymphoid organs (15), according to the schedule shown in Fig. 3*A*. FTY720 stock solution (10 mg/mL in DMSO) was diluted to a 125 μg/mL concentration in PBS directly before administration. Mice received a dose of 10 μg FTY720 or PBS containing

DMSO as control, 3 times per week throughout the experiment via oral gavage.

Spheroid Preparation and Microfluidic Culture. Fresh tumor specimens were excised and placed in media (DMEM) on ice and minced in a 10-cm dish (on ice) using sterile forceps and scalpel. Minced tumor was resuspended in DMEM (4.5 mM glucose, 100 mM Na pyruvate, 1:100 penicillin–streptomycin; Corning CellGro, Manassas, VA) containing 10% FBS (Gemini Bio-Products, West Sacramento, CA), 100 U/mL collagenase type IV (Life Technologies, Carlsbad, CA), and 15 mM Hepes (Life Technologies, Carlsbad, CA). Samples were pelleted and resuspended in 10 to 20 mL media. Red blood cells were removed from visibly bloody samples using RBC Lysis Buffer (Boston BioProducts, Ashland, MA). Samples were pelleted and then resuspended in fresh DMEM containing 10% FBS and strained over 100-μm and 40-μm filters to generate S1 (>100 μm), S2 (40 to 100 μm), and S3 (<40 μm) spheroid fractions, which were subsequently maintained in ultra-low-attachment tissue culture plates. S2 fractions were used for ex vivo culture. An aliquot of the S2 fraction was pelleted and resuspended in type I rat tail collagen (Corning, Corning, NY) at a concentration of 2.5 mg/mL after addition of 10× PBS with phenol red with pH adjusted to 7.0 to 7.5, confirmed using PANPEHA Whatman paper (Sigma-Aldrich, St. Louis, MO). The spheroid-collagen mixture was then injected into the center gel region of the 3D microfluidic culture device. Collagen hydrogels containing MDOTS were hydrated with media with or without indicated therapeutic monoclonal antibodies after 30 min at 37 °C. MDOTS were treated with isotype control IgG (10 μg/mL, clone 2A3) or anti–PD-1 (10 μg/mL, clone RMP1-14).

Live/Dead Staining. Dual labeling was performed by loading a microfluidic device with Nexcelom ViaStain AO/PI Staining Solution (Nexcelom, CS2-0106). After incubation with the dyes (20 min at room temperature in the dark), images were captured on a Nikon Eclipse 80i fluorescence microscope equipped with Z-stack (Prior) and CoolSNAP CCD camera (Roper Scientific). Image capture and analysis were performed using NIS-Elements AR software package. Image deconvolution was done using AutoQuant Module. Whole-device images were achieved by stitching in multiple captures. Live and dead cell quantitation was performed by measuring total cell area of each dye.

RNAseq Analysis. Tumor immune infiltrating $CD45^+$ cells from a responder and a nonresponder mouse were loaded into the 10× Genomics Chromium Controller. The 10× Genomics libraries were prepared following manufacturer's instructions and sequenced on an Illumina HiSeq 2500 sequencer. We obtained single-cell transcriptomes for 2,580 cells from the nonresponder mouse and 4,425 cells from the responder mouse, with an average of 57,000 reads per cell. Demultiplexing, mapping, and gene counting were performed with Cell Ranger 1.1.0 from 10× Genomics, and Seurat 2.2.0 was used for further processing. We filtered out cells that had less than 1,000 or more than 5,000 genes detected (*SI Appendix*, Fig. S3, violin plots with nGene, nUMI and percent mito), keeping 2,552 nonresponder cells and 4,346 responder cells. The data were normalized using the Seurat LogNormalize method and a scale factor of 1e4. Data were scaled using the Seurat function ScaleData. Variable genes were selected with the FindVariableGenes function, using the following cutoffs: x.low.cutoff = 0.0125, x.high.cutoff = 7, y.cutoff = 0.5, producing 1,830 genes for subsequent PCA analysis. The Seurat FindClusters function (using the first 15 PCA components and resolution 0.8) identified 10 clusters. T-distributed Stochastic Neighbor Embedding (t-SNE) plot was executed with the RunTSNE function, using the first 15 PCA components, and cells were colored based on function.

To align the cells from both mice and obtain clusters that reflect the cell type and not the difference in their response to the tumor, we performed a CCA with Seurat following the Seurat tutorial (https://satijalab.org/seurat/immune_alignment.html). In this analysis, we excluded cells with fewer than 1,000 genes detected and with more than 0.15% of mitochondrial gene expression (*SI Appendix*, Fig. S3, violin plots of nGene, nUMI, percent.mitoc), keeping 2,557 nonresponder cells and 4,339 responder cells. We used the union of the top 1,000 variable genes in each dataset (1,356 genes in total) to run the CCA analysis (RunCCA), setting num.cc to 30. We aligned the 2 datasets using the AlignSubspace function, (with options reduction.type=cca, dims.align = 1:30). We ran tSNE analysis (with options reduction.use = cca. aligned, dims.use = 1:20). We identified clusters with FindClusters with the same RunTSNE settings and resolution set to 0.6. These aligned analyses were used to make the dotplot figures.

Bulk RNAseq analysis was performed on MC38 cancer cells isolated from 2 responder and 2 nonresponder mice. To prepare libraries for RNAseq, the TruSeq stranded mRNA protocol was followed as described in the kit (Illumina, USA; RS-122-2101) manual. The 40-nt-long single end reads were mapped to the canonical mouse genome, release mm10, with STAR (43), using an annotation file from ENSEMBL GRCm38.91. Reads were assigned to genes with FeatureCounts (44) using -s 2 and the same gtf file used in the mapping. Read normalization and differential expression were performed with DESeq2 (45).

Statistics. All statistical analysis was performed with Prism software (GraphPad Software), and statistical significance was concluded where $P < 0.05$ (*). For Fig. 5*B*, a 2-way ANOVA, followed by Sidak's multiple comparisons test, was performed to determine significance between each of the conditions (the experiment had 2 variables and 4 conditions).

ACKNOWLEDGMENTS. We thank Jennifer Love, Amanda Chilaka and Sumeet Gupta of the Whitehead Institute Genome Technology Core for technical assistant with RNA sequencing experiments. We thank George Bell of the Whitehead Institute bioinformatics and research-computing group for his critical reading of the manuscript and comments on the bioinformatics analysis. We also thank the flow cytometry and sorting facility at the Whitehead Institute. We thank Irina Mazo and Ulrich H. von Andrian of the Harvard Department of Immunology for technical assistance with enumeration of $CD8^+$ T cells in popliteal lymph nodes. We thank Russell Jenkins for helpful discussions. We also thank W. Nicholas Haining (Dana-Farber Cancer Institute) for providing the MC38 tumor cell line. Funding was provided by American Cancer Society postdoctoral fellowship (M.R.), 1K22CA226040-01 (M.R.), NIH fellowship T32 CA207021 (M.W.L.), Ludwig Fund for Cancer Research (A.D.), Susan G. Komen Postdoctoral Fellowship No. PDF15301255 (Y.Z.), Evergrande Center for Immunologic Diseases and Ludwig Center at Harvard Medical School (A.H.S.), Expect Miracles Foundation and Robert and Renee Belfer Foundation (C.P.P, C.J.L., and A.R.A.), P50CA101942 and P01AI056299 (G.J.F.), R01-AI087879 (H.L.P.), the Melanoma Research Alliance (award ID 51009; H.L.P.), the Lustgarten Foundation (H.L.P.), P01 CA080111 (R.A.W.), and the Ludwig Fund for Cancer Research (R.A.W.).

1. P. Allavena, A. Sica, G. Solinas, C. Porta, A. Mantovani, The inflammatory microenvironment in tumor progression: The role of tumor-associated macrophages. *Crit. Rev. Oncol. Hematol.* **66**, 1–9 (2008).
2. D. Hanahan, L. M. Coussens, Accessories to the crime: Functions of cells recruited to the tumor microenvironment. *Cancer Cell* **21**, 309–322 (2012).
3. J. A. Joyce, D. T. Fearon, T cell exclusion, immune privilege, and the tumor microenvironment. *Science* **348**, 74–80 (2015).
4. E. Sato *et al*., Intraepithelial CD8+ tumor-infiltrating lymphocytes and a high CD8+/regulatory T cell ratio are associated with favorable prognosis in ovarian cancer. *Proc. Natl. Acad. Sci. U.S.A.* **102**, 18538–18543 (2005).
5. O. Kawai *et al*., Predominant infiltration of macrophages and CD8(+) T Cells in cancer nests is a significant predictor of survival in stage IV nonsmall cell lung cancer. *Cancer* **113**, 1387–1395 (2008).
6. N. Yamada *et al*., CD8+ tumor-infiltrating lymphocytes predict favorable prognosis in malignant pleural mesothelioma after resection. *Cancer Immunol. Immunother.* **59**, 1543–1549 (2010).
7. M. Rashidian *et al*., Predicting the response to CTLA-4 blockade by longitudinal noninvasive monitoring of CD8 T cells. *J. Exp. Med.* **214**, 2243–2255 (2017).
8. R. Tavaré *et al*., An effective immuno-PET imaging method to monitor CD8-dependent responses to immunotherapy. *Cancer Res.* **76**, 73–82 (2016).
9. T. R. Simpson *et al*., Fc-dependent depletion of tumor-infiltrating regulatory T cells co-defines the efficacy of anti-CTLA-4 therapy against melanoma. *J. Exp. Med.* **210**, 1695–1710 (2013).
10. S. H. Baumeister, G. J. Freeman, G. Dranoff, A. H. Sharpe, Coinhibitory pathways in immunotherapy for cancer. *Annu. Rev. Immunol.* **34**, 539–573 (2016).
11. M. Rashidian *et al*., Noninvasive imaging of immune responses. *Proc. Natl. Acad. Sci. U.S.A.* **112**, 6146–6151 (2015).
12. M. Rashidian *et al*., The use of ^{18}F-2-fluorodeoxyglucose (FDG) to label antibody fragments for immuno-PET of pancreatic cancer. *ACS Cent. Sci.* **1**, 142–147 (2015).
13. M. Rashidian *et al*., Enzyme-mediated modification of single-domain antibodies for imaging modalities with different characteristics. *Angew. Chem. Int. Ed. Engl.* **55**, 528–533 (2016).
14. S.-R. Woo *et al*., Immune inhibitory molecules LAG-3 and PD-1 synergistically regulate T-cell function to promote tumoral immune escape. *Cancer Res.* **72**, 917–927 (2012).
15. C. Halin *et al*., The S1P-analog FTY720 differentially modulates T-cell homing via HEV: T-cell-expressed S1P1 amplifies integrin activation in peripheral lymph nodes but not in Peyer patches. *Blood* **106**, 1314–1322 (2005).
16. S. Spranger *et al*., Mechanism of tumor rejection with doublets of CTLA-4, PD-1/PD-L1, or IDO blockade involves restored IL-2 production and proliferation of CD8(+) T cells directly within the tumor microenvironment. *J. Immunother. Cancer* **2**, 3 (2014).
17. F. O. Martinez, S. Gordon, The M1 and M2 paradigm of macrophage activation: Time for reassessment. *F1000Prime Rep.* **6**, 13 (2014).
18. R. Noy, J. W. Pollard, Tumor-associated macrophages: From mechanisms to therapy. *Immunity* **41**, 49–61 (2014).
19. J. L. Guerriero, Macrophages: The road less traveled, changing anticancer therapy. *Trends Mol. Med.* **24**, 472–489 (2018).

20. A. R. Aref *et al*., 3D microfluidic ex vivo culture of organotypic tumor spheroids to model immune checkpoint blockade. *Lab Chip* **18**, 3129–3143 (2018).
21. R. W. Jenkins *et al*., *Ex vivo* profiling of PD-1 blockade using organotypic tumor spheroids. *Cancer Discov.* **8**, 196–215 (2018).
22. A. Dongre *et al*., Epithelial-to-mesenchymal transition contributes to immunosuppression in breast carcinomas. *Cancer Res.* **77**, 3982–3989 (2017).
23. A. Brenot, B. L. Knolhoff, D. G. DeNardo, G. D. Longmore, SNAIL1 action in tumor cells influences macrophage polarization and metastasis in breast cancer through altered GM-CSF secretion. *Oncogenesis* **7**, 32 (2018).
24. S. Terry *et al*., New insights into the role of EMT in tumor immune escape. *Mol. Oncol.* **11**, 824–846 (2017).
25. A. Butler, P. Hoffman, P. Smibert, E. Papalexi, R. Satija, Integrating single-cell transcriptomic data across different conditions, technologies, and species. *Nat. Biotechnol.* **36**, 411–420 (2018).
26. Y. Zhang, W. Du, Z. Chen, C. Xiang, Upregulation of PD-L1 by SPP1 mediates macrophage polarization and facilitates immune escape in lung adenocarcinoma. *Exp. Cell Res.* **359**, 449–457 (2017).
27. A. Gratchev *et al*., Alternatively activated macrophages differentially express fibronectin and its splice variants and the extracellular matrix protein betaIG-H3. *Scand. J. Immunol.* **53**, 386–392 (2001).
28. Y. Fujiwara *et al*., Guanylate-binding protein 5 is a marker of interferon-γ-induced classically activated macrophages. *Clin. Transl. Immunology* **5**, e111 (2016).
29. S. J. Im *et al*., Defining CD8+ T cells that provide the proliferative burst after PD-1 therapy. *Nature* **537**, 417–421 (2016).
30. M. J. Trifilo, C. C. Bergmann, W. A. Kuziel, T. E. Lane, CC chemokine ligand 3 (CCL3) regulates CD8(+)-T-cell effector function and migration following viral infection. *J. Virol.* **77**, 4004–4014 (2003).
31. M. E. Keir, L. M. Francisco, A. H. Sharpe, PD-1 and its ligands in T-cell immunity. *Curr. Opin. Immunol.* **19**, 309–314 (2007).
32. J. Lee, E. Ahn, H. T. Kissick, R. Ahmed, Reinvigorating exhausted T cells by blockade of the PD-1 pathway. *For. Immunopathol. Dis. Therap.* **6**, 7–17 (2015).
33. M. M. Gubin *et al*., High-dimensional analysis delineates myeloid and lymphoid compartment remodeling during successful immune-checkpoint cancer therapy. *Cell* **175**, 1014–1030.e19 (2018).
34. P. C. Tumeh *et al*., PD-1 blockade induces responses by inhibiting adaptive immune resistance. *Nature* **515**, 568–571 (2014).
35. G. Siu *et al*., The human T cell antigen receptor is encoded by variable, diversity, and joining gene segments that rearrange to generate a complete V gene. *Cell* **37**, 393–401 (1984).
36. M. M. Davis, P. J. Bjorkman, T-cell antigen receptor genes and T-cell recognition. *Nature* **334**, 395–402 (1988).
37. J. Li *et al*., Genomic segmental polymorphisms in inbred mouse strains. *Nat. Genet.* **36**, 952–954 (2004).
38. A. Marazioti *et al*., Beneficial impact of CCL2 and CCL12 neutralization on experimental malignant pleural effusion. *PLoS One* **8**, e71207 (2013).
39. T. Lu *et al*., Tumor-infiltrating myeloid cells induce tumor cell resistance to cytotoxic T cells in mice. *J. Clin. Invest.* **121**, 4015–4029 (2011).
40. S. Ostrand-Rosenberg, P. Sinha, Myeloid-derived suppressor cells: Linking inflammation and cancer. *J. Immunol.* **182**, 4499–4506 (2009).
41. X. Song *et al*., CD11b+/Gr-1+ immature myeloid cells mediate suppression of T cells in mice bearing tumors of IL-1beta-secreting cells. *J. Immunol.* **175**, 8200–8208 (2005).
42. M. J. W. D. Vosjan *et al*., Conjugation and radiolabeling of monoclonal antibodies with zirconium-89 for PET imaging using the bifunctional chelate p-isothiocyanatobenzyl-desferrioxamine. *Nat. Protoc.* **5**, 739–743 (2010).
43. A. Dobin *et al*., STAR: Ultrafast universal RNA-seq aligner. *Bioinformatics* **29**, 15–21 (2013).
44. Y. Liao, G. K. Smyth, W. Shi, FeatureCounts: An efficient general purpose program for assigning sequence reads to genomic features. *Bioinformatics* **30**, 923–930 (2014).
45. M. I. Love, W. Huber, S. Anders, Moderated estimation of fold change and dispersion for RNA-seq data with DESeq2. *Genome Biol.* **15**, 550 (2014).